

# Near-field acoustic and piezoresponse microscopy of domain structures in ferroelectric material

Q. R. YIN\*, H. R. ZENG, H. F. YU, G. R. LI

State Key Lab of High Performance Ceramics and Superfine Microstructure, Shanghai Institute of Ceramics, Chinese Academy of Sciences, 1295 Dingxi Road, Shanghai 200050, China  
E-mail: qryin@sunm.shcnc.ac.cn

Three kinds of near-field microscopy imaging mode including SEAM (Scanning electron acoustic microscopy), PFM (Piezoresponse force microscopy) and SPAM (Scanning probe acoustic microscopy) have been developed to investigate domain structures of ferroelectric ceramics, crystals and thin films in our studies. The domain imaging mechanisms are presented individually in three imaging modes. Sub-surface micro-domain configuration of ferroelectric BaTiO<sub>3</sub> ceramics and single crystal and their dynamic behavior under external fields were clearly visualized by SEAM. Ferroelectric domain structures of ferroelectric PZT thin film and PMN-PT single crystal were characterized by PFM. Nanoscale switching behavior and local field-induced nanoscale displacement behavior of domain structures in ferroelectric thin film were studied by PFM. Antiparallel domain patterns in ferroelectric transparent PLZT ceramics were also characterized by SPAM. The combination of SEAM, PFM and SPAM in application to imaging domain structures undoubtedly enrich our understanding of the nature of piezoelectricity and ferroelectricity at submicro-, even nano-meter scale.

© 2006 Springer Science + Business Media, Inc.

## 1. Introduction

Piezoelectric and ferroelectric materials have been widely used in microelectronics and micro mechanical application fields due to their piezoelectric, ferroelectric, pyroelectric effects, and so on [1, 2]. These properties and application background are closely related to the domain structure of ferroelectrics and their dynamic behavior under different conditions. Thus *in-situ* imaging and characterization of domain structure with high resolution are very important and imperative to understand local ferroelectric phenomena in ferroelectric materials. In the present study, three kinds of near-field microscopy imaging mode including SEAM (Scanning electron acoustic microscopy), PFM (Piezoresponse force microscopy) and SPAM (Scanning probe acoustic microscopy) have been implemented based on the commercial SEM and AFM, and used to perform studies of domain structures and their dynamic behavior under external fields.

## 2. Experimental

### 2.1. Scanning electron acoustic microscopy

Scanning electron acoustic microscopy (SEAM) is a technique which can produce images that show variations in an object's thermal and elastic properties with a resolution on the order of microns [3–7]. The SEAM system was shown in Fig. 1. SEAM was installed on a conventional SEM KYKY-1000B by attaching an electron beam chopping system consisting of a pair of deflection plates, an electron beam blanking power, a square-wave signal generator, a PZT and a signal preamplifier EG&G Model 5316A with a lock-in amplifier Model 5302. A computer control system was also established to allow the control of the scanning parameter, image capturing and image processing. The electron acoustic image (EAI) and secondary electron image (SEI) can be obtained simultaneously. The physical processes involved in electron acoustic microscopy are shown in Fig. 2. A periodically

\* Author to whom all correspondence should be addressed.

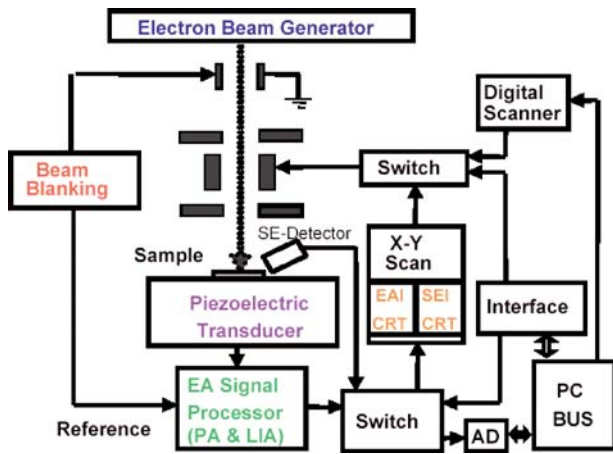


Figure 1 The schematic of scanning acoustic electron microscope.

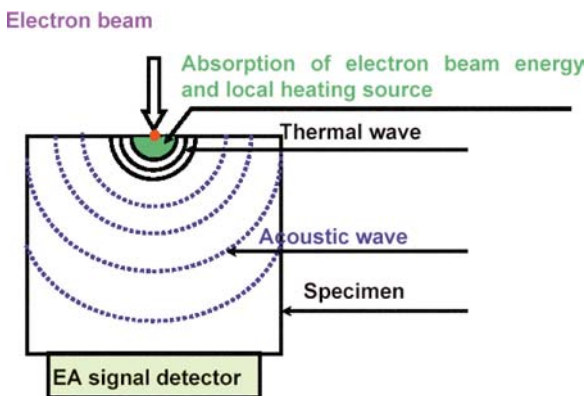


Figure 2 A diagram for physical principle of SEAM.

chopped electron beam serves as a local probe on materials being examined, causing periodic heating and local thermal expansion in the dissipation volume. The periodic expansion and contraction produce acoustic waves that propagate through the sample and are detected by a piezoelectric transducer coupled to the sample. Spatial

variations or discontinuities in any of these thermal and elastic properties produce contrast in the EAI.

### 2.2. Piezoresponse force microscopy

Piezoresponse force microscopy (PFM) has now been used as a powerful tool for imaging and characterization of nanoscale domain structures in ferroelectrics [8–12]. PFM in our studies was developed based on the commercially available atomic force microscope instrument (Seiko SPA 300/SPI3800). The working principle for PFM in imaging domain structures are shown in Fig. 3, where an ac-voltage  $V_{ac} = V_0 \sin \omega t$  is applied between the conductive tip and the bottom electrode of the sample. Due to the converse piezoelectric effect, the alternating external electric field gives rise to the piezoelectric vibration of the sample, or a change in the sample's local thickness. The sign of piezoelectric coefficient depends on the polarization direction, and thus the regions with opposite polarization states will vibrate out of phase upon the action of the ac field. The amplitude and phase of the vibration signal provide information about the magnitude of the piezoelectric coefficient and the direction of local polarization, respectively. Therefore, regions with opposite polarization directions, which vibrate in counter phase with respect to each other under the applied ac field, will appear as regions of different contrasts in the piezoresponse image.

### 2.3. Scanning probe acoustic microscopy

The experimental set up of the scanning probe acoustic microscopy (SPAM) is shown in Fig. 4. The SPAM is a modified commercial atomic force microscope [13]. An ac voltage is applied between the bottom electrode of the piezoelectric sample and the conducting tip. The tip acts as a local excitation source of acoustic waves due to the converse piezoelectric effects. The induced acoustic

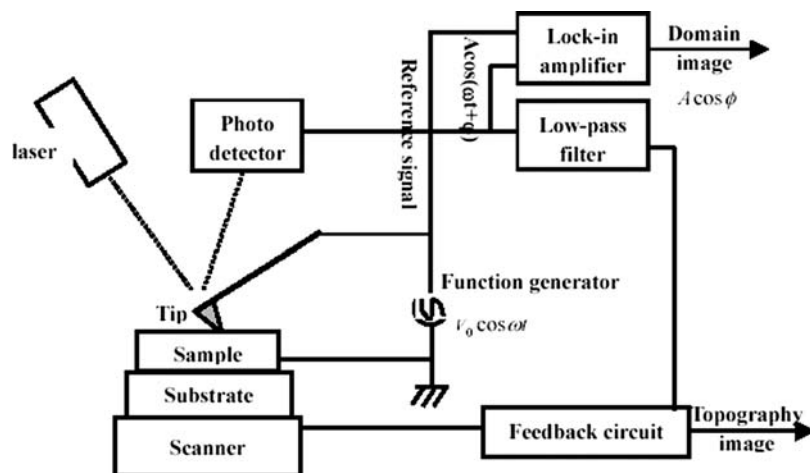


Figure 3 The schematic of piezoresponse force microscope.

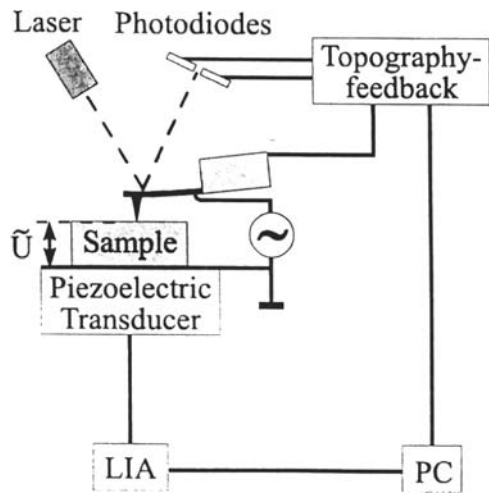


Figure 4 The set up of scanning probe acoustic microscope.

waves are detected by a piezoelectric transducer that is in intimate contact with the bottom surface of the sample. A PC unit is installed to *in-situ* process samples topography and acoustic imaging. In this work, only longitudinal acoustic waves were detected.

### 3. Results and discussion

#### 3.1. Scanning electron acoustic microscopy of ferroelectric domain

##### 3.1.1. Electron acoustic image of sub-surface micro-domain configuration in $\text{BaTiO}_3$ ceramics

Fig. 5a is the SEI of surface topography of  $\text{BaTiO}_3$  ferroelectric ceramics without any pretreatment. The SEI only shows the grain and grain boundaries of  $\text{BaTiO}_3$  ceramics. Fig. 5b–d are the corresponding EAI of the same area at different modulation frequencies. The electron acoustic images exhibit  $90^\circ$  domain configurations with different orientation occurring in the individual  $\text{BaTiO}_3$  grains, as symbol “S” indicated in Fig. 5b. Some domain structures cross in the grain boundaries of the neighboring grains, as symbol “Q” shows in Fig. 5b. The domain-crossing grain boundary phenomena are also clearly seen in Fig. 5e and f. Based on the SEAM imaging principle [14], the EAIs at different modulation frequencies reflect microstructure information at different depth profile away from the sample surface. As a result, the square and circle symbol in Fig. 5b–d represent sub-surface domain configuration in  $\text{BaTiO}_3$  ceramics. So SEAM provides a nondestructive

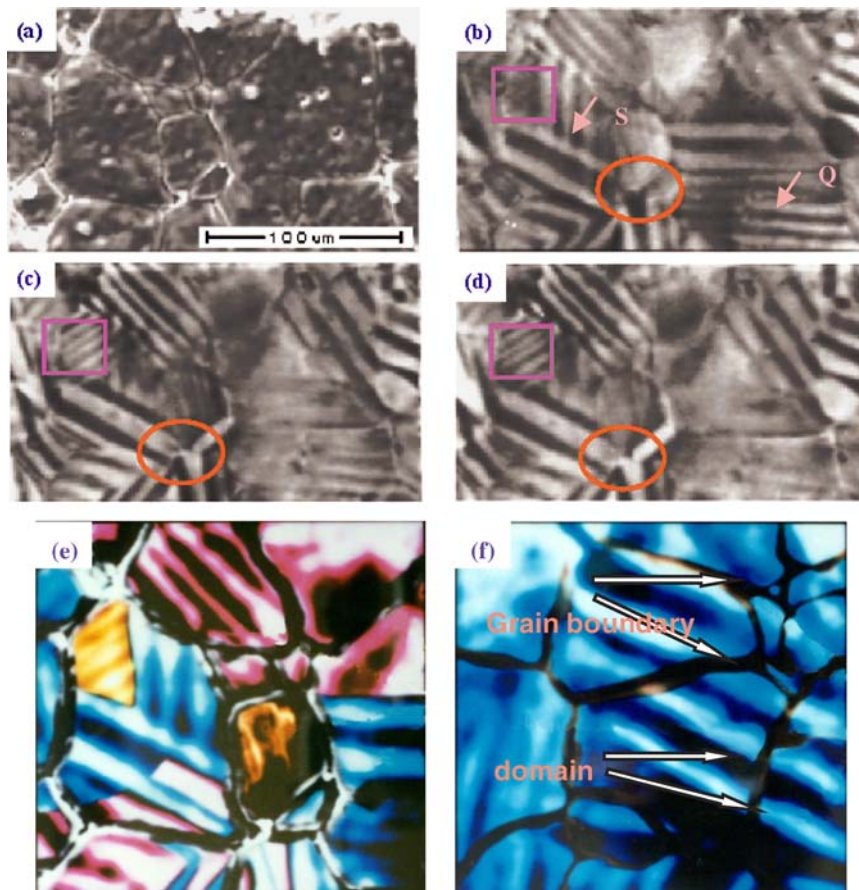


Figure 5 SEI of  $\text{BaTiO}_3$  ceramics, (a) EAI at different modulation frequencies of  $f = 98.9$  kHz, (b)  $114.7$  kHz (c) and  $133.7$  kHz, (d) respectively (e) and (f) showing domain structure crossing the grain boundary of  $\text{BaTiO}_3$  ceramics.

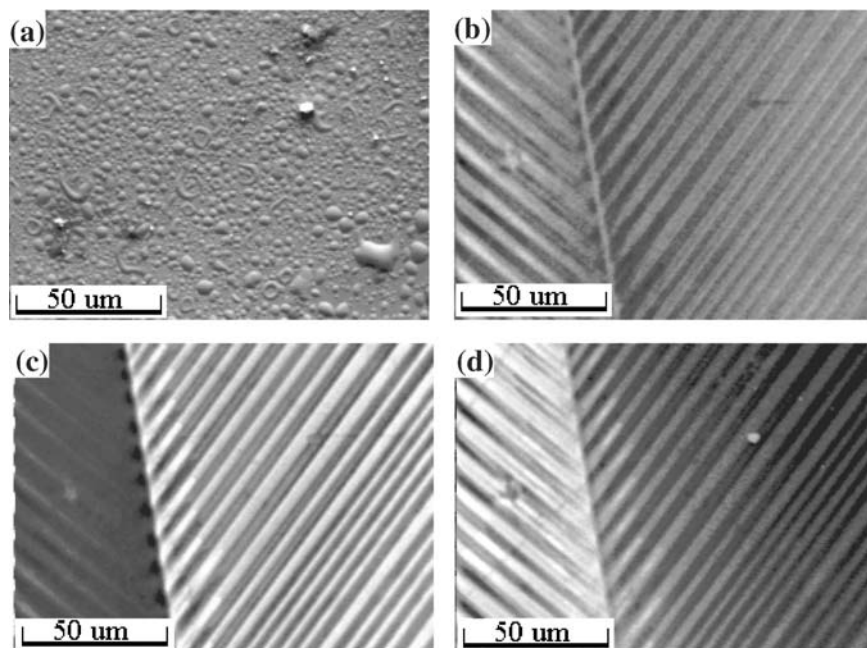


Figure 6 Modulation frequency dependence of domain structure in BaTiO<sub>3</sub> single crystal. (a) SEI, (b) EAI at 79.7 kHz, (c) EAI at 80.6 kHz, and (d) EAI at 132.7 kHz.

tool to image subsurface domain structures in ferroelectric materials through modulating imaging frequency.

### 3.1.2. Modulation frequency dependence of ferroelectric domain imaging contrasts

Fig. 6a is the SEI of the surface morphology of BaTiO<sub>3</sub> single crystals. Fig. 6b–d are the corresponding EAI of BaTiO<sub>3</sub> single crystals at modulation frequencies of 79.7, 80.6, and 132.7 kHz, respectively. The electron acoustic image contrasts of domain structures in Fig. 6b–d reveal an interesting frequency dependence of domain contrasts. In Fig. 6b, both domain groups contribute nearly the same degree of domain contrasts. But in Fig. 6c, strong and sharp contrasts appear in the domain group at the right side, and the left-side domain contrasts are suppressed. When the modulation frequency is increased to 132 kHz, the domain contrasts at right side of Fig. 6d are suppressed, while the left-side domain contrasts show very strong and sharp imaging contrasts. From the above results, we proposed that frequency characteristics of EAI of ferroelectric domain might be related to the frequency resonant properties of domain structures.

### 3.1.3. Domain structures dynamic behavior under electric fields and temperature fields

The domain evolution of 0.65PMN-0.35PT single crystal under external electric fields are shown in Fig. 7

[14]. Fig. 7a is the initial domain configuration when external field  $E = 0$ . There are two groups of domains with different orientations in the figure. The domains shown in Fig. 7b–d evolve gradually with increasing electric field  $E$  perpendicular to the sample surface. All domains coalesce together when electrical field reaches 7.2 kV/cm. It approaches to a single domain state. Actually some micro-domains distributing in the macro-domains might be observed if enhancing SEAM's resolution. The results indicate that the proper poling conditions can be designed for exploring performance of PMN-PT crystal.

Fig. 8a is an EAI that shows the macroscopic ferroelectric domains present in a sample at room temperature prior to annealing [15]. The macrodomains have the well-defined lamellar morphology of tetragonal 90° domains. Fig. 8b demonstrates that the tetragonal 90° macrodomain structure still exists after the annealing process. Generally speaking, no ferroelastic domain structure was observed in the sample prior to annealing, but this was not the case after annealing. Many complex domain structures were found on the surface of the annealed sample, as illustrated in Fig. 8c and d. The twofold symmetrical butterfly-shaped domains with alternate black and white contrasts are clearly revealed in the EAIs Fig. 8c and b. The butterfly-shaped domains pattern was supposed to be due to ferroelastic domains induced by dislocations, and might regarded as ferroelastic domains induced by the presence of dislocations in the crystal formed during the slow cool step of the cooled annealing process.

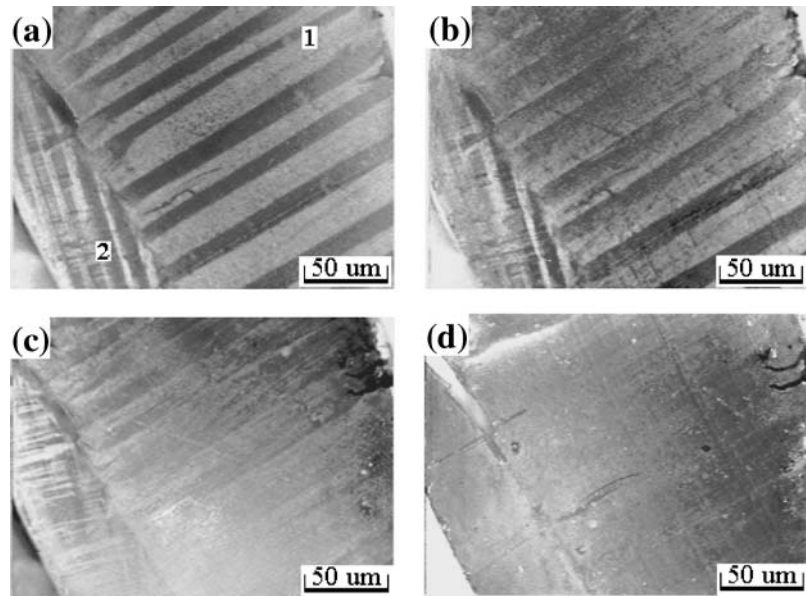


Figure 7 Domain evolution on 0.65 PMN-0.35PT crystal in poling process. (a) EAI at 133.3 kHz,  $E = 0$ ; (b) 133.1 kHz,  $E = 4.5$  kV/cm; (c) 133.4 kHz,  $E = 5.4$  kV/cm; and (d) 133.4 kHz,  $E = 7.2$  kV/cm.

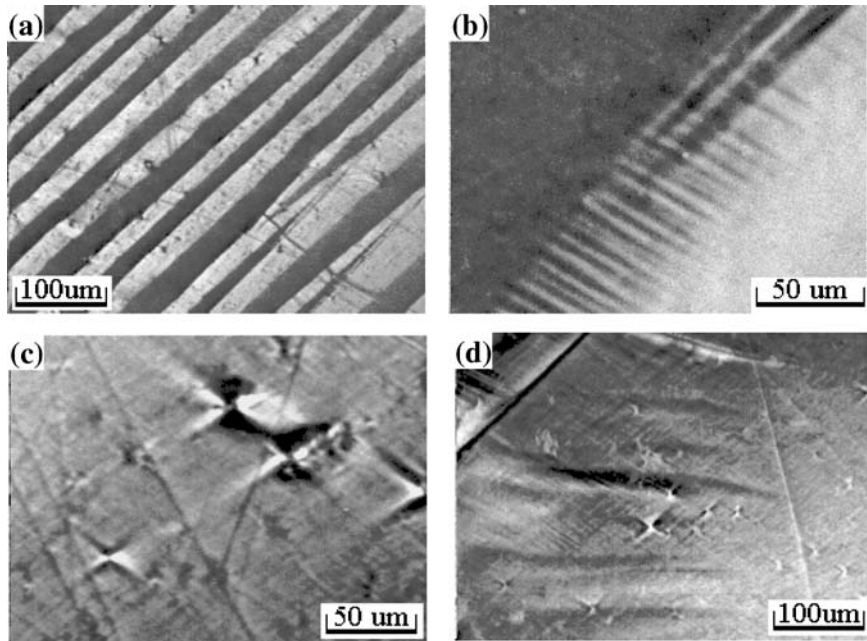


Figure 8 The comparison of ferroelectric domain structures of 0.65 PMN-0.35PT single crystal before (a) and after annealing (b) at 154.8 kHz; (c) and (d) are EAI image of the butterfly shaped domain structure in the annealed 0.65 PMN-0.35 PT single crystals at 154.8 and 153.2 kHz, respectively.

### 3.2. Piezoresponse force microscopy of ferroelectric domain

#### 3.2.1. Piezoresponse image of domain structures in ferroelectric PZT thin film

Fig. 9a shows a topographic image of as-deposited  $\text{Pb}_{0.40}\text{Zr}_{0.60}\text{TiO}_3$  thin film with 300 nm thickness, which reveals a polycrystalline structure with  $\sim 200$  nm sized grains. A corresponding piezoresponse image is shown

in Fig. 9b, where the areas appearing as bright and dark contrasts were undoubtedly  $180^\circ$  domain with antiparallel polarization direction, as indicated in Grain 1 and 2 of Fig. 9, which were usually visualized in many PFM studies of ferroelectric thin films. But interestingly,  $90^\circ$  domain configurations with 80–100 nm in width presenting stripe contrasts were clearly shown in Fig. 9b, as shown in Grain 3 of Fig. 9. The similar phenomena were remarkably

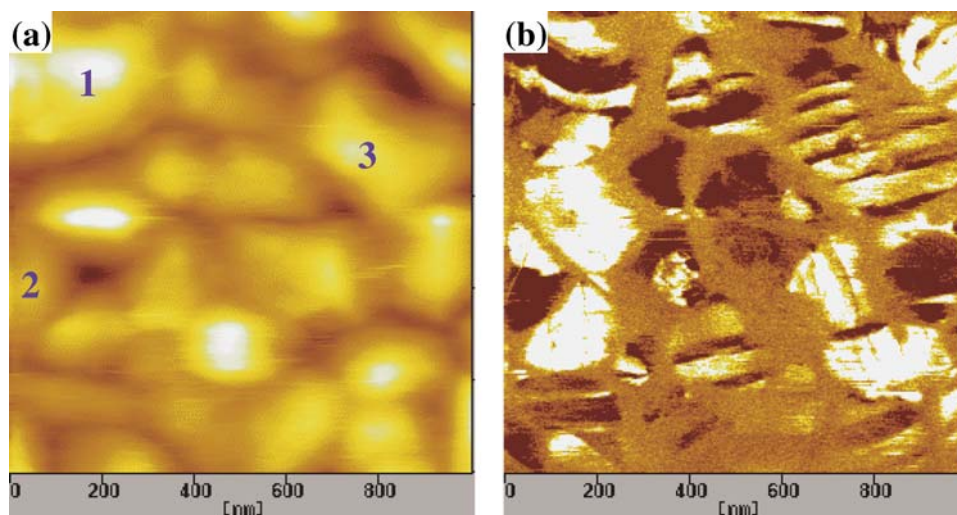


Figure 9 The topography image (a) and the corresponding piezoresponse image (b) of ferroelectric PZT thin film.

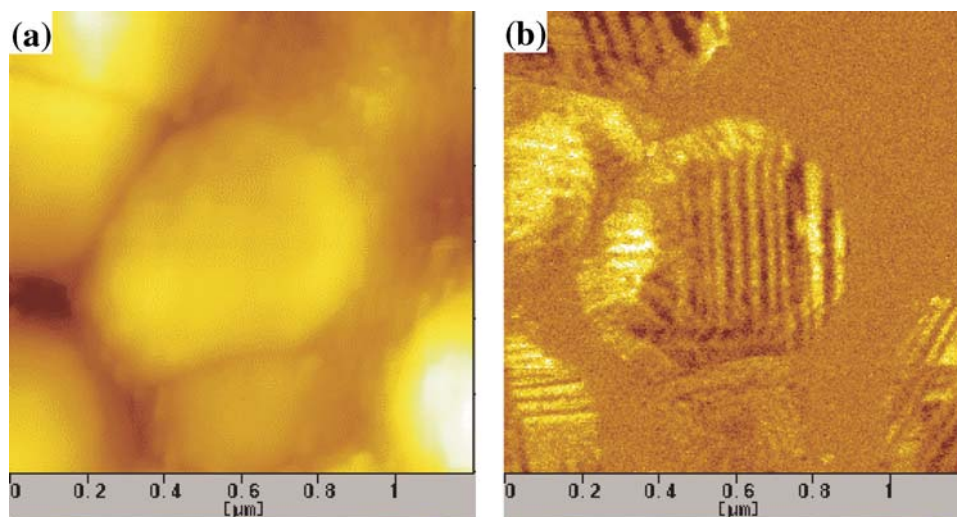


Figure 10 The topography image (a) and the corresponding piezoresponse image (b) of ferroelectric PZT thin film.

demonstrated in Fig. 10.  $90^\circ$  domain structures as small as 30 nm in size were clearly observed in the individual grains of Fig. 10b. Noted that the grains dominated with  $90^\circ$  domain walls are separated from each other in Fig. 10, so grain-clamping effect can be excluded, and nanoscale  $90^\circ$  domain configuration are induced by the periodic lattice constant mismatch between the substrate and the film. It is believed that the local mechanical stress is the predominant cause of the extensive equal-width domain configuration, which is compatible with the periodic stress inside the grains in the film.

### 3.2.2. Piezoresponse image of domain structures in PMN-PT single crystals

Fig. 11a and b show the topography and domain images of the investigated (001)-oriented PMN-30%PT single

crystals. The topography image of Fig. 11a only represents the surface image of the sample without any additional information. The piezoresponse image contrast in Fig. 11b is determined by the out-of-plane component of polarization, where black and white areas correspond to the opposite polarization directions. Irregular, fingerprint-like domain patterns with average size of 200 nm were clearly observed in Fig. 11b. The remarkable contrasted domain regions are not uniform but a mixture of small domain regions with opposite contrasts. The irregular domain patterns are not the unique features of the domain structures visualized in the sample. Another type of regular domain structure was surprisingly imaged in other scanning areas of the same PMN-30%PT single crystal, as shown in Fig. 11c and d. Fig. 11c shows the regular, narrow strip-like domain patterns as compared with irregular those in Fig. 11b, while narrow strip-like domain

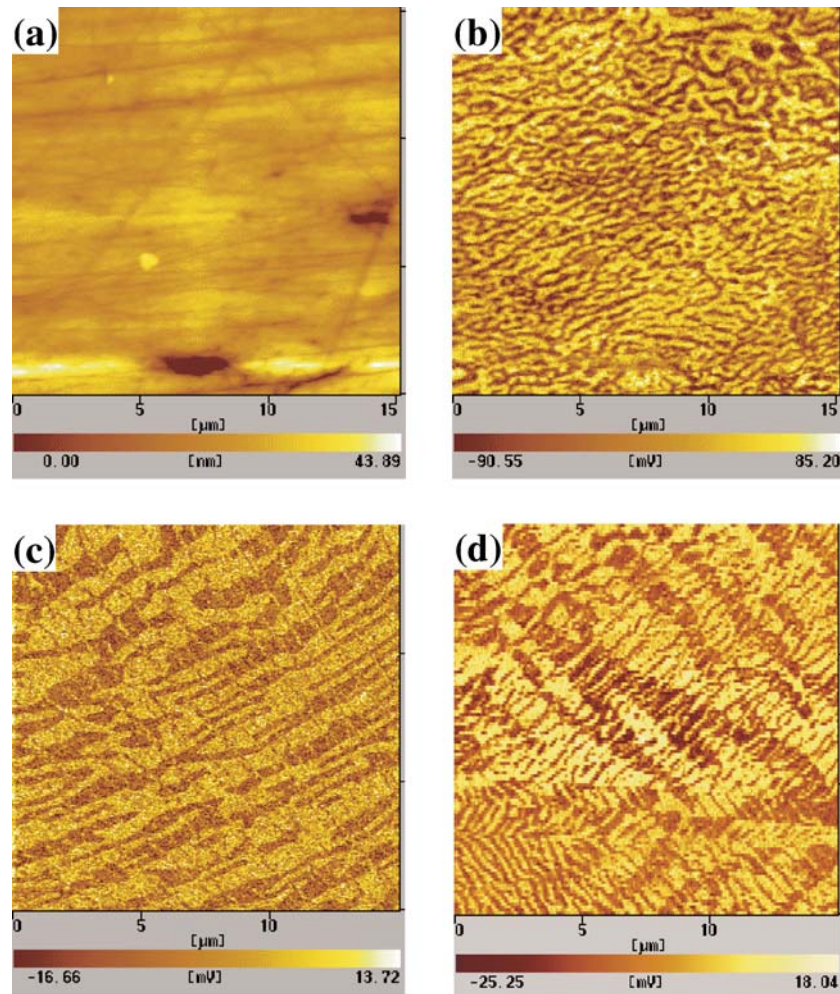


Figure 11 The spatially inhomogeneity of domain structure in PMN-PT single crystal. (a) the topography image and (b) the corresponding piezoresponse image of  $15 \times 15 \mu\text{m}^2$  scanning areas. (c) and (d) are the piezoresponse image in different scanning areas of PMN-PT single crystal.

pattern and finger print domain configuration appear simultaneously in Fig. 11d. The spatially inhomogeneity of domain structure in PMN-PT single crystals reflect that random fields from nanoscale structure irregularity affect greatly the domain arrangement of PMN-PT single crystals [16].

Fig. 12a is the piezoresponse image of domain configurations in (110)-oriented PMN-PT single crystal. The fingerprint domain patterns and the tweed-like domain patterns are simultaneously visualized in the piezoresponse image. The former is the antiparalle, non-ferroelastic domain, and the latter ferroelastic domain structures. A question arises is that what is the relationship between them. Fig. 12b shows that the gradual transition regions between non-ferroelastic domain (fingerprint pattern) and ferroelastic domain (tweed pattern) appearing in PMN-PT single crystal, which reveals that dynamic transformation behavior from non-ferroelastic to ferroelastic domain existing in the crystal due to the local stress during cooling process from high temperatures [17].

### 3.2.3. Nanoscale domain switching behavior in PZT thin film

The polarization reversal behavior of the PZT 40/60 thin film at the nanometer scale was studied with SFM in order to gain a better understanding domain switching mechanism in ferroelectric thin films. The  $5 \times 5 \mu\text{m}^2$  area was successively scanned with the tip bias of  $-1.5 \text{ V}$  and  $+1.5 \text{ V}$ . Immediately after each application of the bias, the SFM piezoresponse mode was used to image the area to obtain simultaneously the topographic image and the corresponding piezoresponse image. Fig. 13a is the topographic image of the PZT 40/60 thin film, showing a dense polycrystalline structure with an average lateral grain size of  $\sim 180 \text{ nm}$ . The corresponding piezoresponse image after application of  $-1.5 \text{ V}$  and  $+1.5 \text{ V}$  are shown in Fig. 13b and c, respectively. The most significant differences in comparison of Fig. 13b with c are the formation of step structure as arrows indicated in Fig. 13c, but not in Fig. 13b. In addition, the step width is found nearly equal in a grain, and the smallest step width is  $\sim 30 \text{ nm}$ . The presence

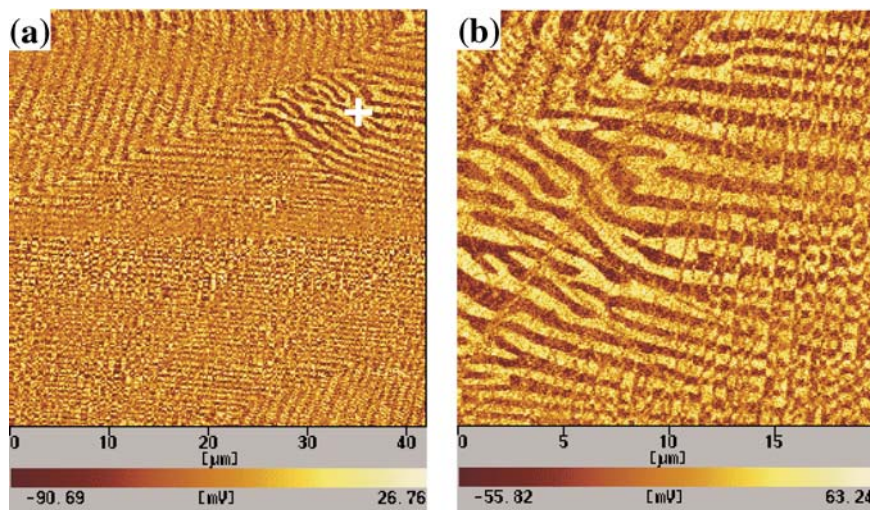


Figure 12 (a) The piezoresponse image of domain structure in PMN-PT single crystal, (b) is the zoomed piezoresponse image with scanning central point located in “+” position marked in Fig. 12a.

of the step domain structure formed during polarization reversal indicates that the domains grow sideways faster than forward in which each of the step doesn't broaden. Our present results substantiate the validity of Hong *et al.*'s claim, i.e. the forward domain growth mechanism being the rate limiting mechanism prevails in our (111) oriented PZT thin films. The presence of the step structure observed by the SFM piezoresponse mode is the reflection of real physical process of nanoscale domain switching [18].

### 3.2.4. Nanoscale displacement behavior of ferroelectric domains

Fig. 14a and b show the topography image and the corresponding piezoresponse image of ferroelectric PZT thin film with graded composition. The field-induced nanoscale displacement behavior of ferroelectric domain was carried out in points A, B, C and D of Fig. 14b. The related results are shown in Fig. 15a–d. Fig. 15a and b clearly exhibit nanoscale displacement-bias butterfly loops of ferroelectric domain under tips, especially typical in Fig. 15a. In contrast, asymmetry butterfly loops were clearly observed in Fig. 15c and d indicates parabola-like loops without any butterfly features.

Based on phenomenological field-induced displacement equation and the displacement-field behavior shown in Fig. 14, it can be deduced that Fig. 15d reflects the square dependence of displacement with electric field due to electrostatic effects. While the hysteresis loop in Fig. 15c implies a combination of piezoelectric and electrostatic effects. For the butterfly displacement-field loops in Fig. 15a and b, we postulate that their origins are from combined contribution of linear piezoelectric effect and domain-switching effect. These combined effects were proposed by Caspari and Merz to explain the macroscopi-

cally strain vs field butterfly loop in bulk BaTiO<sub>3</sub> ceramics [19]. So Caspari-Merz's theory is still valid at nanometer scale.

## 3.3. Scanning probe acoustic microscopy of ferroelectric domain

### 3.3.1. Acoustic image of domain structure in PLZT ceramics

Fig. 16a shows the topography of the PLZT ceramics obtained by SPAM. The main features in the topography are the surface scratches. No information associated with the domain structure was revealed. Fig. 16b is an acoustic image of the PLZT ceramics using the SFM acoustic mode, which clearly reveals fingerprint patterns related to domains structures with antiparallel polarization [14]. These stripes show a pronounced and different contrast in the different areas (A, B, C) appearing in Fig. 16b due to different crystallographic orientations of the individual grains. The bend and split of the domain marked by arrows at the grain boundary regions may be attributed to the existence of inhomogeneous lattice distortions or spatial defects which destroyed the continuity of ferroelectric domains and minimized the elastic energy and depolarization fields at the grain boundaries. The fingerprint patterns in Fig. 16b are relatively regular and are almost periodically spaced in each individual grain. The stripe-structures in Fig. 16b are 300 nm in width.

Fig. 17 illustrates the spatial distribution of the phase difference signal  $\cos \phi$  ( $\phi$ —phase difference between the modulation voltage and the piezoresponse signal). The phase difference corresponds to the direction of the polarization vector. The phase images indicate that the bright and black domain images can be ascribed to the antiparallel polarization, i.e.  $-c$  and

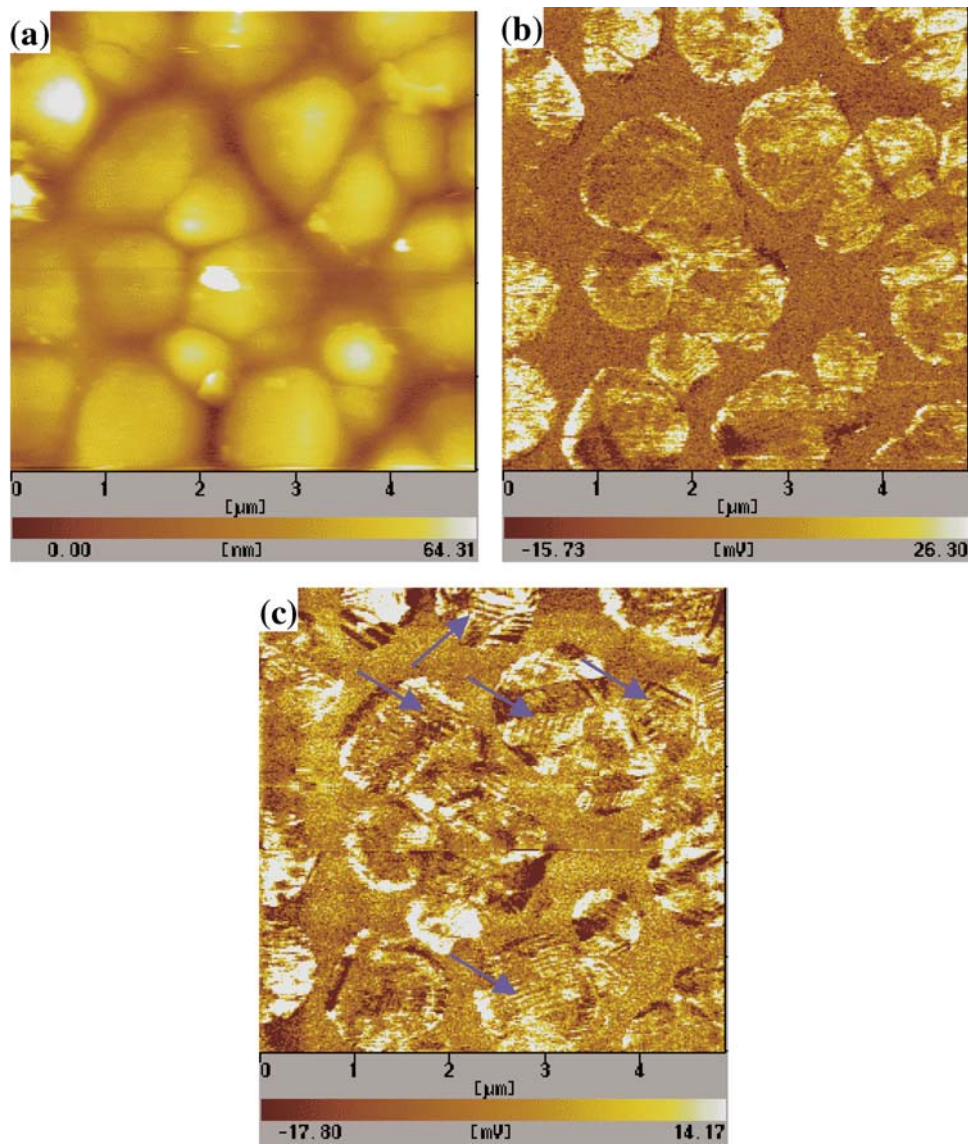


Figure 13 The topographic image (a) and piezoresponse image of  $5 \times 5 \mu\text{m}^2$  regions scanned with tip biased at  $-1.5 \text{ V}$  (b) and  $+1.5 \text{ V}$  (c) in PZT 40/60 thin film.

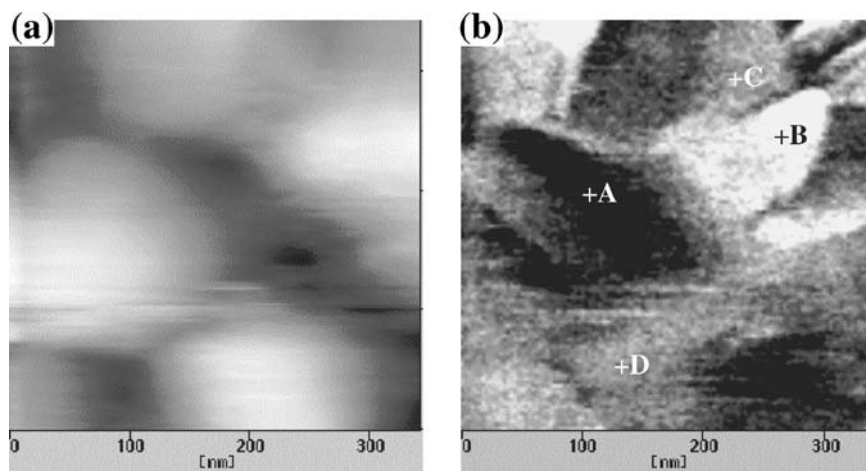


Figure 14 The topography image (a) and the corresponding piezoresponse image (b) of ferroelectric PZT thin film.

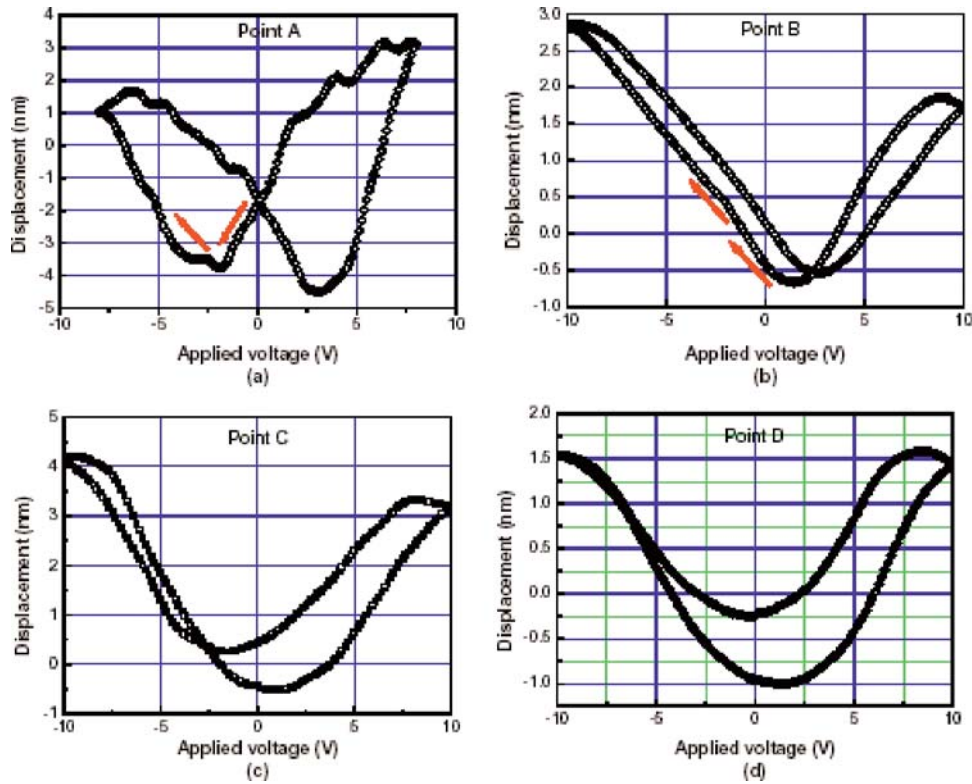


Figure 15 Nanoscale displacement vs electric field hysteresis loop of ferroelectric domains in the point A (a), point B (b), point C (c) and point D (d) shown in Fig. 14b for PZT thin film.

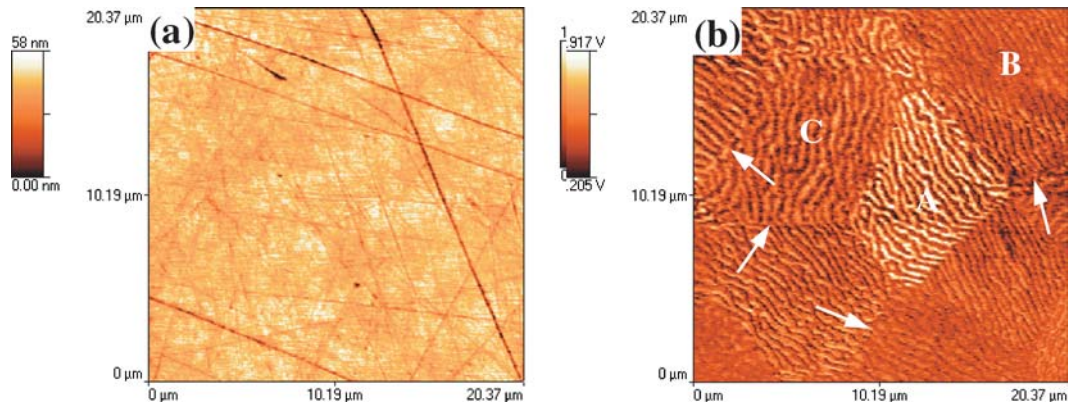


Figure 16 (a) Topography of PLZT ceramics by SFM, and (b) acoustic mode SFM imaging of PLZT ceramics at  $f=131.5$  kHz.

+c domains, respectively. They are consistent with the former analysis, and give confirmation of the observed  $180^\circ$  domain structure in the acoustic image. In addition, the domains appear as bending and splitting patterns at the grain boundaries, as shown in Fig. 16b.

### 3.3.2. Imaging mechanism of antiparallel domains

In SPAM, When an ac voltage is applied between the conductive tip and the rear surface of the sample, the tip acts

as an exciting source and generates acoustic waves in the piezoelectric PLZT ceramics due to the converse piezoelectric effect. Therefore the generation of the acoustic signal in the SPAM is attributed to piezoelectric coupling. The tip has a spherical shape with a radius of curvature of 10 nm, and the excited local region under the tip is about 50 nm in lateral dimensions, 200 nm in depth [4] and is independent of the surrounding area. Each local region of the sample can be considered as an independent piezoelectric vibrator. The vibration model of each piezoelectric vibrator is related to the interaction between the applied electrical field and the polarization vector.

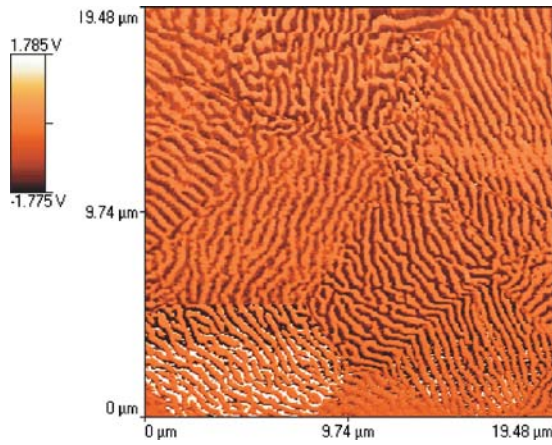


Figure 17 Phase image of acoustic mode SFM scan on PLZT ceramics.

Obviously, this kind of piezoelectric vibration is closely connected with the locally effective piezoelectric constant ( $d_{ij}^{\text{eff}}$ ) of the sample. The effective  $d_{ij}^{\text{eff}}$  piezoelectric tensor is not only related to the piezoelectric coefficients  $d_{31}$ ,  $d_{33}$ ,  $d_{15}$ ,  $d_{22}$  of the PLZT sample which has a La/Zr/Ti ratio of 6/65/35, but also related to the deviation angle of the spontaneous polarization vector from the normal direction (upward) of the sample surface. This composition is in the rhombohedral ferroelectric phase and has eight domain states with spontaneous polarization vectors oriented in the directions of cube diagonals of the cubic

phase. The multi-domain state system with different orientations will give different contribution to the domain contrast observed in the amplitude image in the SFM acoustic mode, which can be considered as an equivalent function of the local effective piezoelectric constants. Different  $d_{ij}^{\text{eff}}$  will undoubtedly give rise to different domain contrast in the acoustic image. For a local area with the spontaneous polarization orientation close to the normal direction of the sample (i.e. nearly parallel to the ac-field direction), its larger  $d_{ij}^{\text{eff}}$  will lead to stronger piezoelectric vibrations and corresponding bright domain tones as shown in the a area of Fig. 16b. In contrast, the local area with larger deviating angle  $\theta$  has a smaller  $d_{ij}^{\text{eff}}$ , thus causing weaker piezoelectric vibrations and showing a gray, dark domain tone, as reflected in the B and C area of Fig. 16b. So the differences in the effective piezoelectric constants of the local areas under the SPAM tip are the intrinsic characteristics resulting in the antiparallel domain contrasts of the PLZT ceramics in SPAM [13].

Fig. 18 shows a magnified acoustic imaging of the stripe-domains. A line scan (A-A') drawn in Fig. 18a is shown in Fig. 18b. The amplitude distribution of the acoustic signal is periodically spaced, reflecting the periodicity of the domain distribution and the homogeneity of the piezoelectricity in PLZT ceramics. In addition, by observing the minimum resolvable peak separation marked by arrows in Fig. 18b, the estimated spatial resolution of acoustic mode SFM imaging in this work is about 70 nm.

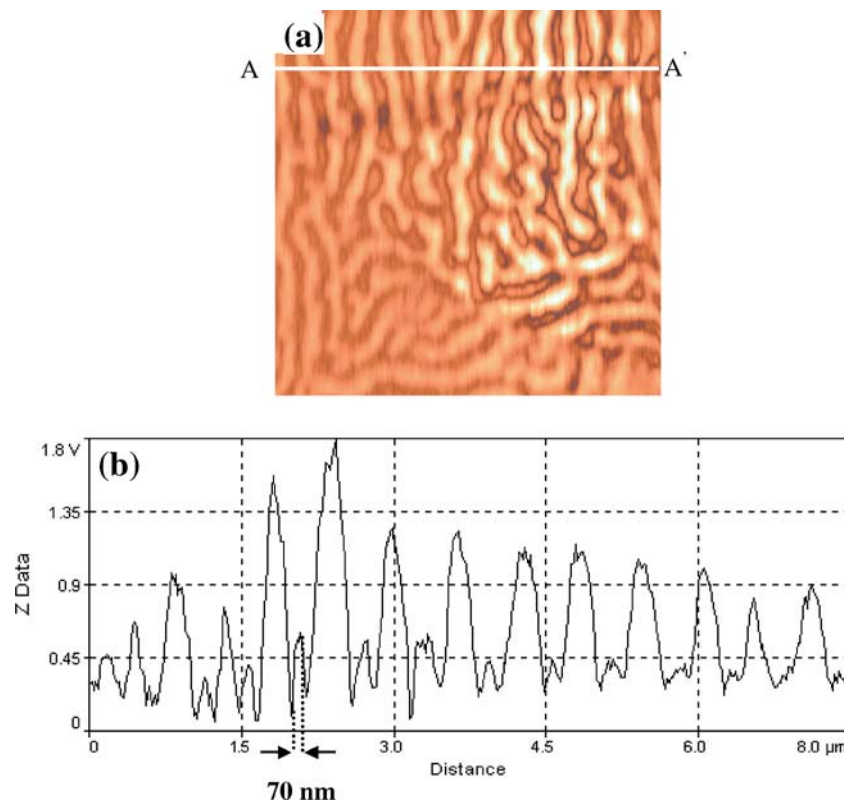


Figure 18 Acoustic mode SFM scan (a) and a line scan (C-D) on PLZT ceramics.

#### 4. Conclusions

In summary, three kinds of near-field microscopy imaging mode including SEAM (Scanning electron acoustic microscopy), PFM (Piezoresponse force microscopy) and SPAM (Scanning probe acoustic microscopy) have been successfully developed based on the commercial SEM and AFM, and used to perform studies of domain structures and their dynamic behavior under external fields in our studies. The domain imaging contrast mechanisms were discussed in terms of their imaging principle, respectively. Sub-surface micro-domain configuration of ferroelectric ceramics and single crystal were clearly visualized by SEAM, and their evolution behavior with dependence of the modulation frequency, temperature and electric field were investigated in details. Ferroelectric domain structures of ferroelectric PZT thin film and PMN-PT single crystal were characterized by PFM. Nanoscale switching behavior and local field-induced nanoscale displacement behavior of domain structures in ferroelectric thin film were studied by PFM. SPAM provides a powerful, non-destructive, near-field imaging tool to explore subsurface domain structures at nanometer scale. Acoustic images of ferroelectric transparent PLZT clearly reveal domain arrangement associated with polarization modulations and homogeneity in the samples. The combination of SEAM, PFM and SPAM in application to imaging domain structures undoubtedly enrich our understanding the nature of piezoelectricity and ferroelectricity at submicro-, even nano-meter scale.

#### References

1. D.L. POLLA and L.F. FRANCIS, *Annu. Rev. Mater. Sci.* **28** (1998) 563.

2. J.F. SCOTT, *Fer. Rev.* **1** (1998) 1.
3. E. BRANDIS and A. ROSENCWAIG, *Appl. Phys. Lett.* **37** (1980) 98.
4. Q. R. YIN, F. M. JIANG and S. X. HUI, *Ferroelectrics*, **151** (1994) 97.
5. B. Y. ZHANG, F. M. JIANG, Y. YANG and Q. R. YIN, *J. Appl. Phys.* **80** (1996) 1916.
6. Idem., *Appl. Phys. Lett.* **70** (1997) 589.
7. M. L. QIAN, X. M. WU, Q. R. YIN, B. Y. ZHANG and J. M. CANTRELL, *J. Mater. Res.* **14** (1999) 3096.
8. A. GRUVERMAN, O. AUCIELLO and H. TOKUMOTO, *Annu. Rev. Mater. Sci.* **28** (1998) 101.
9. C. S. GANPULE, V. NAGARAJAN, B. K. HILL, A. L. ROYTBURD, E. D. WILLIAMS, R. RAMESH, S. P. ALPAY, A. ROELOFS, R. WASER and L. M. ENG, *J. Appl. Phys.* **91** (2002) 1477.
10. V. NAGARAJAN, A. ROYTBURD, A. STANISHIEVSKV, S. PRASERTCHOUNG, T. ZHAO, L. CHEN, J. MELNGAILIS, O. AUCIELLO and R. RAMESH, *Nat. Mater.* **2** (2003) 43.
11. H. R. ZENG, H. F. YU, R. Q. CHU, G. R. LI, H. S. LUO and Q. R. YIN, *J. Cryst. Growth* **267** (2004) 194–198.
12. S. V. KALININ and D. A. BONNELL, *Phys. Rev. B* **65** (2002) 125408.
13. Q. R. YIN, G. R. LI, H. R. ZENG, X. X. LIU, R. HEIDERHOFF and L. J. BALK, *App. Phys. A* **78** (2004) 699.
14. Q. R. YIN, H. R. ZENG, S. X. HUI and Z. K. XU, *Mater. Sci & Eng. B* **99** (2003) 2.
15. J. LIAO, X. P. JIANG, G. S. XU, H. S. LUO and Q. R. YIN, *Mater. Character* **44** (2000) 453.
16. H. R. ZENG, H. F. YU, R. Q. CHU, G. R. LI and Q. R. YIN, *Mater. Letter* **59** (2005) 2380.
17. H. F. YU, H. R. ZENG, R. Q. CHU, G. R. LI and Q. R. YIN, *J. Phys. D. App. Phys.* **21** (2004) 2914.
18. H. R. ZENG, G. R. LI, Q. R. YIN and Z. K. XU, *App. Phys. A* **76** (2003) 401.
19. M.E. CASPARI and W.J. MERZ, *Phys. Rev. B* **80** (1950) 1082.